

# High-Order Adaptive Extended Stencils FEM with Linear Elements\*

Rebecca Conley<sup>†</sup>      Tristan j. Delaney<sup>†</sup>      xiangmin Jiao<sup>†‡</sup>

December 3, 2024

## Abstract

The finite element methods are powerful tools for solving partial differential equations on complex geometries, but their high-order generalizations pose significant challenges in terms of robustness and mesh generation. In this paper, we introduce a high-order finite element method, which is insensitive to element quality and hence is more robust, and which requires only linear elements even for curved geometries and hence significantly simplifies meshing. This method is based on our recent work on *Adaptive Extended Stencil FEM*, or *AES-FEM* (*Int. J. Num. Meth. Engrg.*, 2016, DOI:10.1002/nme.5246). AES-FEM replaces the traditional interpolatory FEM basis functions with *generalized Lagrange polynomial basis functions*, constructed via local weighted-least-squares approximations. AES-FEM overcomes the element quality dependence of FEM, while preserving its basic theoretical framework. In this work, we address some key issues in extending AES-FEM to high order, in terms of the selection of stencils, the analysis of its accuracy, and the resolution of curved geometries. We show that even-degree polynomials are in general preferred for even-order PDEs, and that linear elements are sufficient for AES-FEM over curved geometries. We present numerical results in 2D and 3D for the Poisson equation and the time-independent convection-diffusion equation. Our results demonstrate up to sixth order accuracy with AES-FEM, and show that AES-FEM is much easier to use than FEM for curved boundaries, while being more accurate, more stable, and more efficient in terms of runtime versus error over sufficiently fine meshes.

**Key Words:** finite element methods; partial differential equations; curved boundaries; high-order accuracy; stability; weighted least squares

65N30; 65N12

---

<sup>†</sup>This work was partially supported by DoD-ARO under contract #W911NF0910306 and also in part by a subcontract to Stony Brook University from Argonne National Laboratory under Contract DE-AC02-06CH11357 for the SciDAC program funded by the Office of Science, Advanced Scientific Computing Research of the U.S. Department of Energy.

<sup>‡</sup>Dept. of Applied Math. & Stat., Stony Brook University, Stony Brook, NY 11794, USA.

<sup>3</sup>Corresponding author. Email: xiangmin.jiao@stonybrook.edu.

# 1 Introduction

Finite element methods (FEM) are one of the most important tools for solving partial differential equations on complex geometries. FEM originated as a second-order accurate method. For several decades, researchers have been exploring “high-order” variants with third or greater order accuracy. Some high-order methods include isoparametric FEM [12],  $hp$ -FEM [10], discontinuous Galerkin methods [8], spectral element methods [6], and isogeometric analysis [17]. Despite the fact that these methods can reach high-order convergence under appropriate conditions, they have remained largely confined to academic research and have yet to make much of an impact in industry [36]. This is due to many reasons, not the least of which are robustness [38] and mesh generation [26]. It is well known that the traditional FEM have a strong dependence on element quality: even just a few “bad” elements can result in ill-conditioned stiffness matrices and hence slow convergence of iterative solvers or loss of accuracy. This problem is even more acute for high-order methods, because most high-order FEM methods require curved elements along boundaries [4], and it difficult to ensure the geometric validity of these elements, especially in 3D [14].

In this paper, we propose a robust, high-order finite element method, which significantly alleviates the requirements on mesh generation. Our approach is based on the *adaptive extended stencil finite element method* or *AES-FEM* (pronounced “ace”-F-E-M) [9]. AES-FEM replaces the piecewise polynomial Lagrange basis functions of the traditional FEM with *generalized Lagrange polynomial (GLP) basis functions*, constructed using weighted-least squares over adaptively extendable stencils. AES-FEM overcomes the element-quality dependence of the FEM, and allows the use of poorly-shaped elements without compromising accuracy, stability, and efficiency, while preserving the theoretical framework of FEM. In the high-order extension, we utilize linear elements for numerical integration and efficient construction of stencils. We show that it suffices to use linear elements for high-order convergence in AES-FEM even for curved geometries. Therefore, it significantly simplifies mesh generation. In addition, we show that even-degree polynomials are in general preferred for AES-FEM when solving elliptic and parabolic PDEs that are even order. We present numerical results in 2D and 3D for the Poisson equation and the time-independent convection-diffusion equation. Our results demonstrate up to sixth order accuracy with AES-FEM, and show that AES-FEM is much easier to use than FEM, while being more accurate, more stable, and more efficient in terms of runtime versus error over finer meshes.

The remainder of the paper is organized as follows. Section 2 discusses the background and some related methods. Section 3 presents the basic formulation of AES-FEM. Section 4 addresses some key issues in extending AES-FEM to high-order accuracy. Section 5 presents the numerical results to assess its accuracy, stability, and efficiency. Section 6 concludes the paper with a discussion on future work.

## 2 Background and Related Work

In this section, we review some high-order finite element methods and contrast them with AES-FEM.

### 2.1 Isoparametric and $hp$ -Adaptive FEM

The isoparametric finite element method uses the same shape functions, often, high-degree polynomials, to define both the geometry and the functional approximations [40, 12]. If the boundary of the domain is curved, then curved elements are necessary for the accurate solution of the geometry for isoparametric FEM [4]. The use of curved elements poses significant challenges in meshing. If an element is too distorted, then a one-to-one mapping between the reference element and the physical element no longer exists, and the method may break down [40]. While progress has been made [19, 35], generating high-order meshes for curved geometries has remained a significant challenge and is still far from being practical, especially in 3D.

While isoparametric FEM in general uses the same-degree polynomial basis uniformly, the degrees of the basis functions may also be adapted, as in the  $p$ -adaptive FEM [33, 2]. The  $p$ -adaptivity may be combined with  $h$ -adaptivity, leading to the  $hp$ -adaptive FEM or  $hp$ -FEM [32, 39]. In these methods, inter-element continuity is typically enforced as constraints [31]. The  $hp$ -FEM can achieve high-order convergence, with error decreasing exponentially in the degree of basis functions, provided that the mesh is nearly optimal [10]. Similar to isoparametric FEM, the  $hp$ -FEM also requires good element shapes for stability, and requires curved elements to resolve curved boundaries to ensure high-order convergence.

In contrast to isoparametric and  $hp$ -adaptive FEM, AES-FEM needs only meshes with linear elements, and its accuracy and stability are independent of element quality. Therefore, AES-FEM circumvents the open problem of generating high-order meshes.

### 2.2 Spectral Element Methods and Discontinuous Galerkin

Spectral methods use infinitely differentiable, global basis functions in the weighted residual formulation for solving differential equations [6]. They can achieve exponential convergence provided the solution is smooth. However, they are not applicable to complex geometries [22]. The spectral element method, which divides the domain into quadrilaterals or hexahedra, was introduced to better handle more general geometries [24]. Generating quadrilateral and hexahedral meshes is very challenging for complex geometries, and hence triangle- and tetrahedron-based spectral element methods have been proposed [34]. Standard Gaussian quadrature cannot be used with triangle spectral element method, and it is still an open question regarding the optimal placements of nodes in triangles and tetrahedra [23]. In contrast, AES-FEM needs only nodes in a linear

FEM mesh for computations and uses standard Gaussian quadrature rules for numerical integrations.

Similar to FEM, discontinuous Galerkin (DG) methods start with a weak form of the governing equation. Continuity of the basis and test functions between elements is not enforced. Instead, a numerical flux is used at the element boundaries. DG methods are able to achieve high-order accuracy and can be used on complex geometries [8]. High-order DG methods have been applied to the Navier-Stokes and compressible Euler equations [4, 3]. Other methods related to DG include the interior penalty methods for elliptical problems, which can be unified with DG under one framework [1], the compact DG [25], which has a more compact stencil than local DG methods, and hybridized DG [7], which has a relatively low number of degrees of freedom. Unlike DG, AES-FEM uses continuous basis functions and test functions.

### 2.3 Isogeometric Analysis and Meshless Methods

Isogeometric analysis (IGA) uses NURBS (Non-Uniform Rational B-Splines) or T-splines as basis functions instead of the standard FEM basis functions [17]. These methods can deliver high accuracy over very coarse meshes and can be advantageous for problems that can benefit from high-degree continuity, such as thin-shell modeling. Another related method is the NURBS-enhanced finite element method (NEFEM), which uses NURBS to represent the boundary of the computational domain and uses standard piecewise polynomials for solutions [28]. These methods bypass the process of generating meshes in the traditional sense, and they can deliver accurate solutions with relatively fewer degrees of freedom. However, they do not alleviate the dependency on mesh quality, because NURBS and T-splines tend to impose a stronger requirement on mesh quality than the traditional FEM.

Another class of methods, which also bypasses mesh generation, is the meshless or meshfree methods [5, 21]. However, these methods tend to be less efficient, typically require special quadrature rules, and suffer from difficulties in the accurate resolution of curved boundaries. In contrast, AES-FEM leverages meshes with linear elements for neighborhood searches and for resolving the boundary, and hence it can enable better accuracy and efficiency, while preserving the overall framework of FEM.

## 3 Formulation of AES-FEM

In this section, we review the formulation of AES-FEM, which was introduced in [9]. We summarize some key results in terms of robustness and accuracy, and refer readers to [9] for more detail.

### 3.1 Weighted Residual Formulation

As most finite element methods, AES-FEM starts from the weighted residual formulation [13]. Consider a linear differential operator  $\mathcal{L}$  defined on a bounded, simply-connected domain  $\Omega$ , with outward unit normal vector  $\mathbf{n}$ . Denote the boundary of  $\Omega$  as  $\Gamma = \Gamma_D \cup \Gamma_N$ , where  $\Gamma_D$  and  $\Gamma_N$  are disjoint sets on which Dirichlet and Neumann boundary conditions are specified, respectively. We want to find a function  $U$  such that

$$\mathcal{L}U = \rho \quad (1)$$

subject to the boundary conditions

$$U = g \text{ on } \Gamma_D \quad \text{and} \quad \frac{\partial U}{\partial \mathbf{n}} = h \text{ on } \Gamma_N. \quad (2)$$

Eq. (1) is the strong form of the PDE. In the weighted residual formulation, we use the weak form based on a set of weight functions  $\Psi = \{\psi_1, \dots, \psi_n\}$ , by requiring the residual  $\mathcal{L}U - \rho$  to be orthogonal to  $\psi_i$ , i.e.,

$$\int_{\Omega} \psi_i (\mathcal{L}U - \rho) \, dV = 0. \quad (3)$$

Typically,  $\Psi$  forms a partition of unity, i.e.,  $\sum_{i=1}^n \psi_i = 1$ , and in this case the weak form satisfies global conservation in the sense of  $\int_{\Omega} (\mathcal{L}U - \rho) \, dV = 0$ .

To approximate  $U$ , let  $\Phi = \{\phi_1, \dots, \phi_n\}$  be a set of basis functions and define an approximation

$$U \approx \sum_{j=1}^n x_j \phi_j. \quad (4)$$

Substituting (4) into the weak form (3) and rearranging the equations, we then obtain

$$\sum_{j=1}^n x_j \int_{\Omega} \psi_i (\mathcal{L}\phi_j) \, dV = \int_{\Omega} \psi_i \rho \, dV, \quad (5)$$

leading to a system of equations in  $x_j$ . If  $\mathcal{L}$  is the Laplacian operator, integration by parts is often used to reduce the order of the derivatives.

If the weight functions are chosen to be the same as the basis functions, then we will arrive at the Galerkin methods. In AES-FEM, we use the standard (“hat”) FEM as test functions, but we construct polynomial basis functions using weighted least squares (WLS), as we discuss next.

### 3.2 Weighted Least Squares Approximations

To compute the basis functions, we begin with multivariable Taylor series expansions. Let us use 2D as an example. Following the discussions as in [18, 37], consider a bivariate function  $f(\mathbf{u})$  with at least  $d + 1$  continuous derivatives in some neighborhood of  $\mathbf{u}_0 = (0, 0)$ . Denote  $c_{jk} = \frac{\partial^{j+k}}{\partial u^j \partial v^k} f(\mathbf{u}_0)$ . Then, for any

$\mathbf{u}$  in the neighborhood,  $f$  may be approximated to the  $(d+1)$ st order accuracy about the origin  $\mathbf{u}_0$  as

$$f(\mathbf{u}) = \underbrace{\sum_{p=0}^d \sum_{j,k \geq 0}^{j+k=p} c_{jk} \frac{u^j v^k}{j! k!}}_{\text{Taylor Polynomial}} + \underbrace{\mathcal{O}(\|\mathbf{u}\|^{d+1})}_{\text{remainder}}. \quad (6)$$

Analogous formulae exist in 1D and 3D. The coefficients  $c_{jk}$  are the unknowns, and we compute them as follows.

We select a stencil of  $m$  nodes from the neighborhood around  $\mathbf{u}_0$ , and locally parameterize the neighborhood such that  $\mathbf{u}_0$  is located at the origin  $(0,0)$ . Substituting the locally parametrized neighboring points into (6), we obtain a set of approximate equations

$$\sum_{p=0}^d \sum_{j,k \geq 0}^{j+k=p} c_{jk} \frac{u_i^j v_i^k}{j! k!} \approx f_i, \quad (7)$$

where  $f_i = f(\mathbf{u}_i)$  and the  $c_{jk}$  denote the unknowns. There are  $n = (d+1)(d+2)/2$  unknowns in 2D and  $n = (d+1)(d+2)(d+3)/6$  unknowns in 3D. Let  $\mathbf{V}$  denote the generalized Vandermonde matrix (i.e., the coefficient matrix of (7)),  $\mathbf{c}$  the vector of unknowns (i.e., the  $c_{jk}$ ), and  $\mathbf{f}$  the right-hand side vector of (7). Then we arrive at an  $m \times n$  rectangular system

$$\mathbf{V}\mathbf{c} \approx \mathbf{f}. \quad (8)$$

To solve (8), we use a weighted linear least-squares formulation [16] to minimize a weighted norm (or semi-norm)

$$\min_{\mathbf{c}} \|\mathbf{V}\mathbf{c} - \mathbf{f}\|_{\mathbf{W}} \equiv \min_{\mathbf{c}} \|\mathbf{W}(\mathbf{V}\mathbf{c} - \mathbf{f})\|_2, \quad (9)$$

where  $\mathbf{W}$  is an  $m \times m$  diagonal weighting matrix, and it is a constant for a given node. Denoting the diagonal entries of  $\mathbf{W}$  as  $w_i$ , the  $i$ th row of matrix  $\mathbf{V}$  is assigned the weight  $w_i$ . We assign heavier weights to nodes that are closer to  $\mathbf{u}_0$ , thus prioritizing them. If  $\mathbf{f}$  is in the range of  $\mathbf{V}$ , then a nonsingular weighting matrix does not affect the solution. If  $\mathbf{f}$  is not in the range of  $\mathbf{V}$ , which is generally the case when  $m > n$ , then prioritizing points can result in better accuracy for smooth functions. In particular, we compute the weights as follows. Let  $h$  denote the maximum radius of the neighborhood, that is

$$h = \max_{1 \leq i \leq m} \{\|\mathbf{u}_i\|_2\}. \quad (10)$$

Then

$$w_i = \left( \frac{\|\mathbf{u}_i\|_2}{h} + \epsilon \right)^{-1}, \quad (11)$$

where  $\epsilon$  is a small constant, such as 0.01, introduced to avoid division by zero.

After the weighting matrix has been applied, we arrive at a new system

$$\mathbf{M}\mathbf{c} \approx \tilde{\mathbf{f}}, \quad \text{where } \mathbf{M} = \mathbf{W}\mathbf{V} \text{ and } \tilde{\mathbf{f}} = \mathbf{W}\mathbf{f}. \quad (12)$$

The matrix  $\mathbf{M}$  may be poorly scaled, which can lead to ill-conditioning of the linear system and in turn potential instability. We employ a diagonal scaling matrix  $\mathbf{S}$  to address the potential issue of poor scaling of  $\mathbf{M}$ . Let  $\mathbf{a}_j$  denote the  $j$ th column of  $\mathbf{M}$ . A typical choice for the  $j$ th entry of  $\mathbf{S}$  is either  $1/\|\mathbf{m}_j\|_2$ , which approximately minimizes the 2-norm condition number of  $\mathbf{MS}$  [16], or  $1/\|\mathbf{m}_j\|_\infty$ . The matrix  $\mathbf{S}$  does not affect the solution mathematically. After the rescaling, the problem becomes

$$\min_{\mathbf{d}} \left\| \tilde{\mathbf{V}}\mathbf{d} - \tilde{\mathbf{f}} \right\|_2, \quad \text{where } \tilde{\mathbf{V}} \equiv \mathbf{W}\mathbf{V}\mathbf{S} = \mathbf{MS} \text{ and } \mathbf{d} \equiv \mathbf{S}^{-1}\mathbf{c}. \quad (13)$$

Conceptually, the solution to the above problem may be reached through the use of a pseudoinverse, and we would have

$$\mathbf{d} = \tilde{\mathbf{V}}^+ \tilde{\mathbf{f}} \quad \text{where } \tilde{\mathbf{V}}^+ \equiv (\tilde{\mathbf{V}}^T \tilde{\mathbf{V}})^{-1} \tilde{\mathbf{V}}^T. \quad (14)$$

Since  $\tilde{\mathbf{V}}$  may still be rank-deficient or ill-conditioned, in practice we solve it using truncated QR factorization with column pivoting, coupled with a condition-number estimator. Finally, we obtain the vector of coefficients  $\mathbf{c}$  for the Taylor polynomial as

$$\mathbf{c} = \mathbf{S}\mathbf{d}. \quad (15)$$

### 3.3 Generalized Lagrange Polynomial Basis Functions

The WLS described above constructs a polynomial approximation given points  $\mathbf{u}_i$  and function values  $f(\mathbf{u}_i)$ . To construct basis functions, we define a generalization of the notion of Lagrange polynomial interpolation. We say the basis functions  $\{\phi_i\}$  constitutes a set of degree- $d$  *generalized Lagrange polynomials (GLP) basis functions* if

1.  $\sum_i f(\mathbf{u}_i) \phi_i$  approximates a smooth function  $f$  to  $\mathcal{O}(h^{d+1})$  in a neighborhood of the stencil, where  $h$  is some characteristic length measure, and
2.  $\sum_i \phi_i = 1$ .

Similarly to Lagrange polynomials, the first property indicates that the physical meanings of the coefficients of the polynomial approximations are the function values, and the second property indicates that the basis functions form a partition of unity. However, the set GLP basis functions allows the number of points to differ from the number of basis functions, and hence it is applicable to least squares approximations.

To construct the GLP basis functions using WLS, let  $\mathcal{P}_k^{(d)}(\mathbf{u})$  denote the set of all  $k$ -dimensional monomials of degree  $d$  and lower, stored in ascending order

as a column vector. For example,  $\mathcal{P}_2^{(2)}(\mathbf{u}) = [1, u, v, u^2, uv, v^2]^T$ . Let  $\mathbf{D}_k^{(d)}$  be a diagonal matrix consisting of the fractional factorial part of the coefficients in the Taylor series corresponding to  $\mathcal{P}_k^{(d)}$ ; for example,  $\mathbf{D}_2^{(2)} = \text{diag}(1, 1, 1, 1/2, 1, 1/2)$ . If there are no ambiguities, we will simply use  $\mathcal{P}$  and  $\mathbf{D}$  as shorthands for  $\mathcal{P}_k^{(d)}$  and  $\mathbf{D}_k^{(d)}$ , respectively. Then, we may write the truncated Taylor series as

$$f(\mathbf{u}) \approx \mathbf{c}^T \mathbf{D} \mathcal{P}(\mathbf{u}). \quad (16)$$

Given the stencil  $\{\mathbf{u}_i\}$  about a point  $\mathbf{u}_0$ , we compute the  $j$ th basis function  $\phi_j$  by letting  $\mathbf{f} = \mathbf{e}_j$  in (8), where  $\mathbf{e}_j$  is the  $j$ th column of the  $n \times n$  identity matrix. Following (14) and (15), we have

$$\mathbf{c}_j = \mathbf{S} \tilde{\mathbf{V}}^+ \mathbf{W} \mathbf{e}_j. \quad (17)$$

Thus the vector  $\mathbf{c}_j$  is exactly the  $j$ th column of  $\mathbf{S} \tilde{\mathbf{V}}^+ \mathbf{W}$ . Therefore, a whole set of basis functions is given by

$$\Phi = \left( \mathbf{S} \tilde{\mathbf{V}}^+ \mathbf{W} \right)^T \mathbf{D} \mathcal{P}. \quad (18)$$

Moreover, as shown in Theorem 2 of [9], the set  $\Phi$  constitutes a set GLP basis functions. The properties of GLP basis functions ensure the consistency of the polynomial approximations in AES-FEM, and also allow the Dirichlet boundary conditions to be imposed easily in the same manner as in the traditional FEM.

## 4 High-Order AES-FEM

The high-order AES-FEM shares the same overall algorithm as the basic AES-FEM in [9]. However, there are some key issues that we must address, including the selection of stencils, the choice of the polynomial degrees, and the resolution of curved boundaries. In this section, we describe the high-order AES-FEM using the Poisson equation as an example, and address the aforementioned issues.

### 4.1 Accuracy of AES-FEM

The AES-FEM described in [9] can achieve high-order accuracy when proper degrees of basis functions are used. For concreteness, let us consider the Poisson equation with Dirichlet boundary conditions as an example, for which the weak form under the weighted-residual formulation is given by

$$\int_{\Omega} \psi_i \nabla^2 U \, dV = \int_{\Omega} \psi_i \rho \, dV. \quad (19)$$

Substituting (4) into (19), we obtain

$$\sum_{j=1}^n x_j \int_{\Omega} \psi_i \nabla^2 \phi_j \, dV = \int_{\Omega} \psi_i \rho \, dV. \quad (20)$$

As in FEM, we use integration by parts to reduce the order of derivatives required by (20). If  $\psi_i$  has weak derivatives and satisfies the condition  $\psi_i|_{\Gamma_D} = 0$ , then after integrating by parts and imposing the boundary conditions, we arrive at

$$-\sum_{j=1}^n x_j \int_{\Omega} \nabla \psi_i \cdot \nabla \phi_j \, dV = \int_{\Omega} \psi_i \rho \, dV. \quad (21)$$

Taking (21) over the  $n$  test functions, we obtain the linear system

$$\mathbf{K}\mathbf{x} = \mathbf{b}, \quad (22)$$

where  $\mathbf{K}$  is the stiffness matrix and  $\mathbf{b}$  is the load vector, with

$$k_{ij} = -\int_{\Omega} \nabla \psi_i \cdot \nabla \phi_j \, dV \quad \text{and} \quad b_i = \int_{\Omega} \psi_i \rho \, dV. \quad (23)$$

In AES-FEM, we use the GLP basis functions for  $\phi_j$ , where the degree of the basis functions may vary. For the test functions  $\psi_i$ , we use the piecewise-linear traditional FEM shape functions, a.k.a. the “hat” functions, independent of the degree of the basis functions. Note that for different  $\psi_i$ , we may use different basis functions, constructed using WLS with different stencils at each node. Therefore, it is possible to adapt the degree of the polynomials for different  $\psi_i$ . In this work, we shall assume that the degree of the basis functions is uniform.

The order of convergence of AES-FEM is determined by the degree of the basis functions, as summarized by Theorem 2 in [9], which we include here for completeness.

**Theorem 1.** *Suppose  $U$  is smooth and thus  $\|\nabla U\|$  is bounded. When solving the Poisson equation using AES-FEM with degree- $d$  GLP basis functions in (21), for each  $\psi_i$  the weak form (19) is approximated to  $\mathcal{O}(h^d)$ , where  $h$  is some characteristic length measure of the mesh.*

Thus the truncation error in the weak form is equal to the degree of the GLP basis functions. We expect the solution to converge at the same rate as the local truncation errors if the method is stable, the rounding errors do not dominate the truncation errors, and there is no systematic cancelation of truncation errors. This is true for even-degree basis functions for Poisson equations, as we will demonstrate in Section 5.

However, when using AES-FEM with odd-degree basis functions, the situation is more complicated. In practice, we observe that if the highest-order spatial derivative of the PDE is even, which is typically the case for elliptic and parabolic PDEs, the order of convergence may be one less than the degree of the basis functions when using odd-degree polynomials. This is because of the cancelation of the odd functions in the integrals over equally spaced grids. To illustrate this effect, let us consider an odd-degree polynomial  $f(x) = x^{2m+1}$ . Suppose the two elements incident on the node at  $x = 0$  are  $[-l_1, 0]$  and  $[0, l_2]$ , and the test function associated the node is  $\psi$ . On an equally spaced grid,

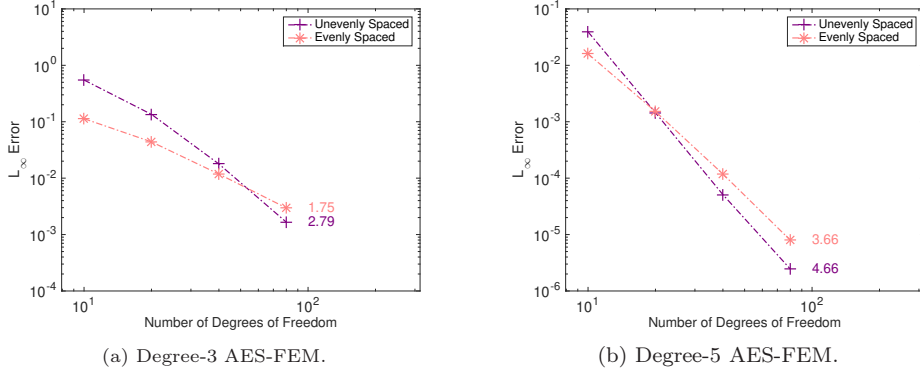


Figure 1: The errors from AES-FEM with odd-degree basis functions for the Poisson equation in 1D. The number to the right of each curve indicates the average convergence rate.

$l_1 = l_2$ ,  $\psi'(x) = -\psi'(-x)$  and  $f'(x) = f'(-x)$ . Therefore,

$$\int_{-l}^0 \psi'(x) f'(x) dx = - \int_0^l \psi'(x) f'(x) dx.$$

Integrating the weak form corresponding to the test function  $\psi$ , we obtain

$$\int_{\Omega} \psi' f' dx = \int_{-l}^l \psi' f' = \int_0^l \psi' f' dx - \int_0^l \psi' f' dx = 0.$$

For nearly even-spaced grids, which is typically the case, the integral corresponding to odd-degree polynomials would be close to zero, so using degree- $(2m + 1)$  polynomials would lead to similar errors as using degree- $2m$  polynomials. Figure 1 demonstrates this behavior numerically with the Poisson equation in 1D using degree-3 and 5 basis functions. It can be seen that on unequally spaced grids, the convergence rate is approximately equal to the degree of polynomials, but for equally spaced grids, the convergence was lower, although the error may be smaller. This behavior can also be observed in 2D and 3D. Therefore, we will use only even-degree basis functions in the weak forms for even-order PDEs. For odd-order PDEs, odd-degree basis functions would be recommended for AES-FEM.

## 4.2 Selection of Stencils

To achieve high-order accuracy, a critical question is the selection of the stencils at each node for the construction of the GLP basis functions. We utilize meshes for speedy construction of the stencils. Given a simplicial mesh (i.e. a triangle mesh in 2D or a tetrahedral mesh in 3D), the *1-ring neighbor elements* of a node are defined to be the elements incident on the node. The *1-ring neighborhood* of a node contains the nodes of its 1-ring neighbor elements [18]. For any

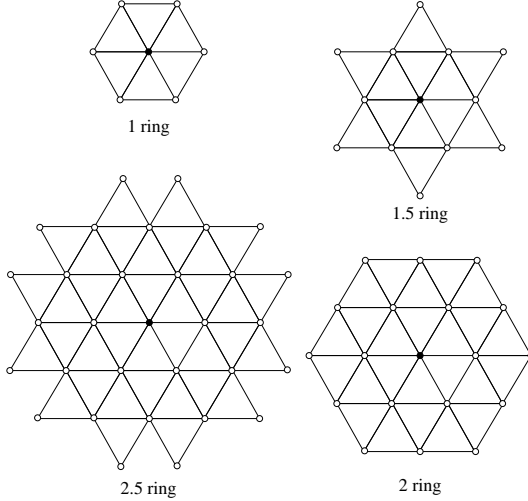


Figure 2: Examples of 2D stencils with 1-ring, 1.5-ring, 2-ring, and 2.5-ring neighborhoods of the center node (in solid black).

integer  $k \geq 1$ , we define the  $(k+1)$ -ring neighborhood as the nodes in the  $k$ -ring neighborhood plus their 1-ring neighborhoods.

The 1-ring neighborhood of a node may supply a sufficient number of nodes for constructing quadratic GLP basis functions. However, 2- and 3-rings are often too large for cubic and quartic constructions. We refine the granularity of the stencils by using fractional rings. In 2D we use half-rings, as defined in [18]. For an integer  $k \geq 1$ , the  $(k + 1/2)$ -ring neighborhood is the  $k$ -ring neighborhood together with the nodes of all the faces that share an edge with the  $k$ -ring neighborhood. See Figure 2 for an illustration of rings and half-rings in 2D. For 3D, we use  $1/3$ - and  $2/3$ -rings, as defined in [9]. For any integer  $k \geq 1$ , the  $(k + 1/3)$ -ring neighborhood contains the  $k$ -ring neighborhood together with the nodes of all elements that share a face with the  $k$ -ring neighborhood. The  $(k + 2/3)$ -ring neighborhood contains the  $k$ -ring neighborhood together with the nodes of all faces that share an edge with the  $k$ -ring neighborhood.

For 2D triangular meshes, the  $1^{1/2}$ -ring has an appropriate number of nodes for quadratic basis functions. The 2-ring,  $2^{1/2}$ -ring, 3-ring, and  $3^{1/2}$ -ring typically provide an appropriate number of nodes for degree 3 to 6 basis functions, respectively. For 3D tetrahedral meshes, the 1-ring,  $1^{1/3}$ -ring,  $1^{2/3}$ -ring, 2-ring, and  $2^{1/3}$ -ring have an appropriate number of nodes for degrees 2 to 6 basis functions, respectively. If a particular neighborhood does not provide enough points, we further expand the stencil to a larger ring. This allows AES-FEM to overcome element-quality dependence and also to improve the stability of its local computations.

To implement the neighborhood search, we need some an efficient mesh data structure. We use the Array-based Half Facet (AHF) data structure [11], of

---

**Algorithm 1** Building Stiffness Matrix and Load Vector Using AES-FEM

---

**input:** 1.  $\mathbf{x}$ , elems, sibhfs, v2hf: half-facet mesh data structure  
2.  $p$ : desired degree for GLP functions  
3.  $\epsilon$ : tolerance for rank deficiency  
4. isDBC: flags for Dirichlet boundary conditions

**output:** stiffness matrix  $\mathbf{K}$  and load vector  $\mathbf{b}$

```
1: for each node without Dirichlet boundary conditions do
2:   obtain neighborhood of node
3:   calculate local parameterization  $\mathbf{x}_k$  and row weights  $\mathbf{w}$  for neighborhood
4:   initialize generalized Vandermonde matrix and factorize
5:   obtain local element neighborhood
6:   for each element incident on the node do
7:     calculate element Jacobian and local coordinates of quad-points
8:     calculate derivatives of FEM shape functions at quad-points
9:      $\mathbf{a} \leftarrow \mathcal{D}\mathcal{P}(\mathbf{x})$ , as needed by the weak form of the PDE
10:    compute GLP basis functions and derivatives
11:    for each node in neighborhood do
12:      if not Dirichlet BC node then
13:        add integral to appropriate stiffness matrix entry
14:      else
15:        subtract integral from load vector
16:      end if
17:    end for
18:    calculate load vector over current element
19:  end for
20: end for
```

---

which the data model is based on the concept of half-facets. In a  $d$ -dimensional mesh, the term *facet* refers to the  $(d-1)$ -dimensional mesh entities; that is, in 2D the facets are the edges, and in 3D the facets are the faces. In a manifold mesh, every facet consists of two half-facets that are oriented in opposite directions. These two half-facets are *sibling half-facets*. Half-facets on the boundary of the domain have no siblings. Each half-facet is identified by a two tuple: the element ID and a local facet ID within the element. In 2D, we store the element connectivity (elems), sibling half-edges (sibhfs), and a mapping from each node to an incident half-edge (v2hf). In 3D, we store the element connectivity (elems), sibling half-faces (sibhfs), and a mapping from each node to an incident half-face (v2hf). Using this data structure, the AES-FEM can be implemented efficiently. Algorithm 1 outlines the key steps of AES-FEM in building the stiffness matrix and the load vector.

### 4.3 Resolution of Curved Geometries

Another critical issue of AES-FEM is the resolution of curved geometries. For isoparametric FEM, it is well known that the elements near the boundary

must be curved and must approximate the boundary to a high enough order [4, 20]. This is because the mid-edge or mid-face nodes of the isoparametric elements must approximate the geometry accurately; otherwise, the geometric errors would dominate and in turn undermine the overall order of convergence of the PDE solutions. In AES-FEM, it is also important for all the nodes to approximate the boundary to high-order accuracy, which is typically the case. However, in contrast to isoparametric FEM, it is sufficient to use linear elements in AES-FEM, even along curved boundaries. This does not compromise the order of convergence of AES-FEM, because in AES-FEM the basis functions are constructed from the nodes, independently of the elements. The linear elements are used only in constructing the piecewise-linear test functions, and to approximate the domain of integration. The effect of this linear approximation of the domain of integration is confined in the approximation to the weak form (3). As a result, instead of solving the weak form (3), we would be solving a perturbed weak form

$$\int_{\tilde{\Omega}} \psi_i (\mathcal{L}U - \rho) \, dV = 0, \quad (24)$$

where the boundary of  $\tilde{\Omega}$  is a piecewise linear approximation to that of  $\Omega$ . Note that (24) remains an exact equality for the exact  $U$  and  $\rho$ . Therefore, Theorem (1) remains valid for the perturbed weak form

$$\int_{\tilde{\Omega}} \psi_i \nabla^2 U \, dV = \int_{\tilde{\Omega}} \psi_i \rho \, dV$$

in place of (19), and the order of convergence is still guaranteed. The only compromise of using the piecewise linear approximation to the boundary is that if the test functions  $\Psi$  forms a partition of unity, the global conservation is satisfied in the sense of  $\int_{\tilde{\Omega}} (\mathcal{L}U - \rho) \, dV = 0$  instead of  $\int_{\Omega} (\mathcal{L}U - \rho) \, dV = 0$ . This slight variation of global conservation in general does not constitute a problem for applications. Note that Neumann boundary conditions may require some different treatments, similar to high-order surface integration [27], which we will address in future work.

## 5 Numerical Results

In this section, we assess the accuracy, efficiency, and element-quality dependence of AES-FEM with quadratic, quartic, and sextic basis functions, and compare it against FEM with linear, quadratic and cubic basis functions. The errors are calculated using the discrete  $L_2$  and  $L_\infty$  norms. Let  $U$  denote the exact solution and let  $\tilde{U}$  denote the numerical solution. Then, we calculate the norms as

$$L_2(\text{error}) = \left( \int_{\Omega} |\tilde{U} - U|^2 \, d\Omega \right)^{1/2} \quad \text{and} \quad L_\infty(\text{error}) = \max_i |\tilde{U} - U|. \quad (25)$$

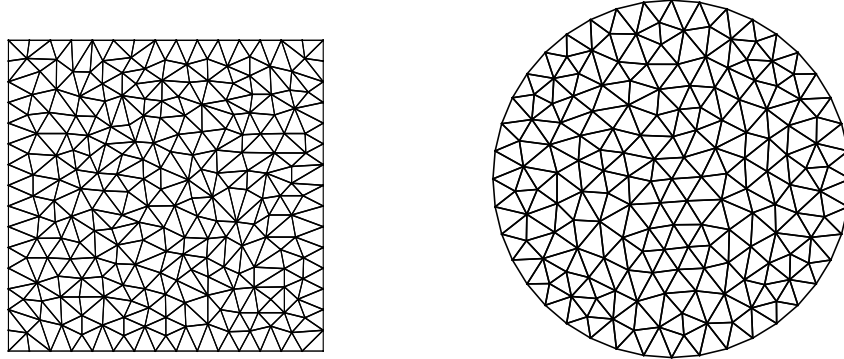


Figure 3: Example 2D meshes with linear elements.

On a series of meshes of different grid resolution, we calculate the average convergence rate as

$$\text{convergence rate} = -\log_2 \left( \frac{\text{error on } m_c}{\text{error on } m_f} \right) \Big/ \log_2 \left( \sqrt[d]{\frac{\text{nodes in } m_c}{\text{nodes in } m_f}} \right), \quad (26)$$

where  $d$  is the spacial dimension,  $m_c$  is the coarsest mesh, and  $m_f$  is the finest mesh.

### 5.1 2D Results

We first assess AES-FEM in 2D over the unit square and the unit circle, which are representative for geometries with flat and curved boundaries, respectively. We triangulated the domains using Triangle [29] for linear meshes and using Gmsh [15] for quadratic and cubic meshes. See Figure 3 for some examples meshes with linear elements, which are representative in terms of mesh quality but are coarser than those used in actual computations. The numbers of nodes for the unit square range from 1,027 to 146,077, and those for the unit circle range from 544 to 79,417. Since isoparametric FEM requires good mesh quality, we ensured that these meshes all have good element shapes for our comparative study: For linear meshes, the minimum angle is 24.04 degrees and the maximum angle is 128.17 degrees; for high-order meshes, all elements have positive Jacobians everywhere.

We consider the Poisson equation and convention-diffusion equation. For both cases, we use GMRES with the ILU preconditioner to solve the linear systems arising from AES-FEM. For FEM, we use conjugate gradient (CG) with incomplete Cholesky as the preconditioner for the Poisson equation, and use GMRES with ILU for the convection-diffusion equation. To demonstrate the accuracy of high-order methods, we set the tolerance of the iterative solvers to  $10^{-12}$ . The drop tolerance for the incomplete factorization is set as  $10^{-4}$  by default, unless otherwise noted.

### 5.1.1 Poisson Equation

We first present results for the Poisson equation with Dirichlet boundary conditions on the unit square and on the unit circle. That is,

$$-\nabla^2 U = \rho \quad \text{in } \Omega, \quad (27)$$

$$U = g \quad \text{on } \partial\Omega. \quad (28)$$

For the unit square  $\Omega = [0, 1]^2$ , we consider the following three analytic solutions:

$$U_1 = 16x^3(1 - x^3)y^3(1 - y^3), \quad (29)$$

$$U_2 = \cos(\pi x) \cos(\pi y), \quad (30)$$

$$U_3 = \frac{\sinh(\pi x) \cosh(\pi y)}{\sinh \pi \cosh \pi}. \quad (31)$$

For the unit circle  $\Omega = \{(x, y) | x^2 + y^2 \leq 1\}$ , we consider  $U_3$  and also

$$U_4 = \cos\left(\frac{\pi}{2}(x^2 + y^2)\right).$$

For each problem, the right-hand side  $\rho$  and the Dirichlet boundary condition  $g$  are obtained from the given analytic solutions. For all the cases, the iterative solvers converged to the desired tolerance for AES-FEM. For FEM, the solver stagnated for the finest meshes in some cases without achieving the specified tolerance, even after we reduced the drop tolerance to  $10^{-6}$  in incomplete Cholesky. However, the resulting errors were small enough not to affect the comparison qualitatively.

Figure 4 shows the  $L_\infty$  and  $L_2$  norm errors for  $U_1$  on the unit square. The  $L_2$  norm errors for  $U_2$  and  $U_3$  on the unit square and for  $U_3$  and  $U_4$  on the unit circle are shown in Figures 5 and 6, respectively. In all cases, quadratic AES-FEM and linear FEM have similar errors, and quartic AES-FEM has similar or better results compared to cubic FEM. Both of the above pairs have similar sparsity patterns and similar numbers of nonzeros in the coefficient matrices. Furthermore, sextic AES-FEM is far more accurate than all the other methods, achieving sixth-order accuracy despite the use of linear elements. This result confirms our accuracy analysis in Section 4 for 2D problems.

### 5.1.2 Convection-Diffusion Equation

In our second example, we consider the time-independent convection-diffusion equation with Dirichlet boundary conditions, that is,

$$-\nabla^2 U + \mathbf{c} \cdot \nabla U = \rho \quad \text{in } \Omega, \quad (32)$$

$$U = g \quad \text{on } \partial\Omega. \quad (33)$$

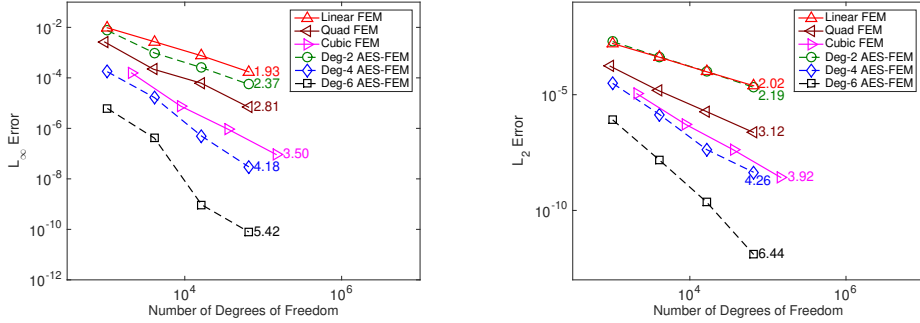


Figure 4: The errors for 2D Poisson equation on the unit square for  $U_1$  in  $L_\infty$  (left) and  $L_2$  norms (right). The number to the right of each curve indicates the average convergence rate.

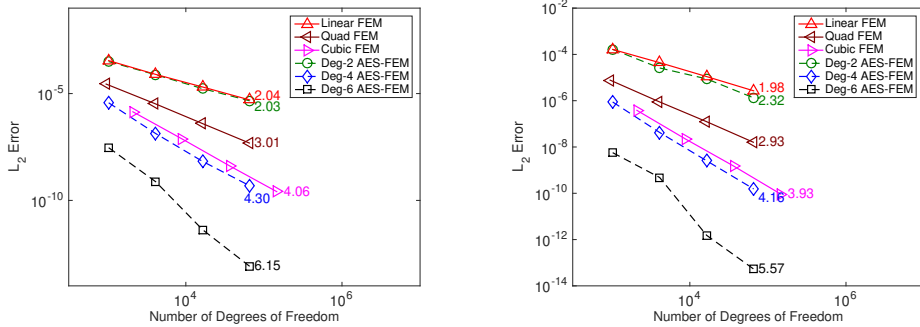


Figure 5: The  $L_2$  norm errors for 2D Poisson equation on the unit square for  $U_2$  (left) and  $U_3$  (right).

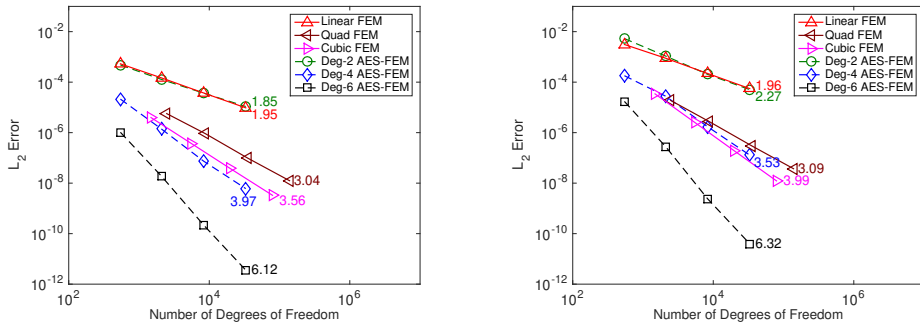


Figure 6: The  $L_2$  norm errors for 2D Poisson equation on the unit circle for  $U_3$  (left) and  $U_4$  (right).

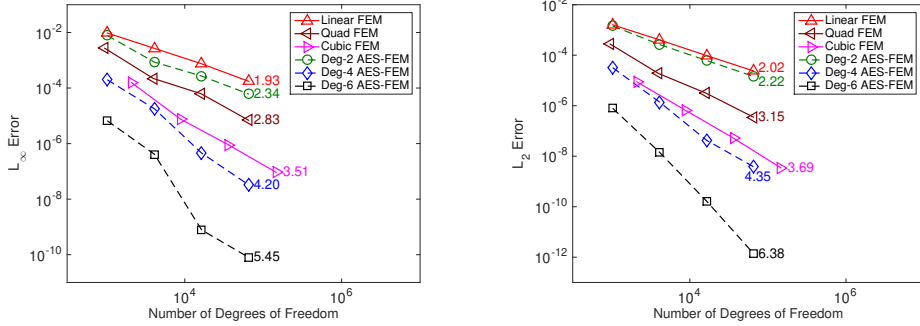


Figure 7: The errors for 2D convection-diffusion equation on the unit square for  $U_1$  in the infinity norm (left) and the  $L_2$  norm (right).

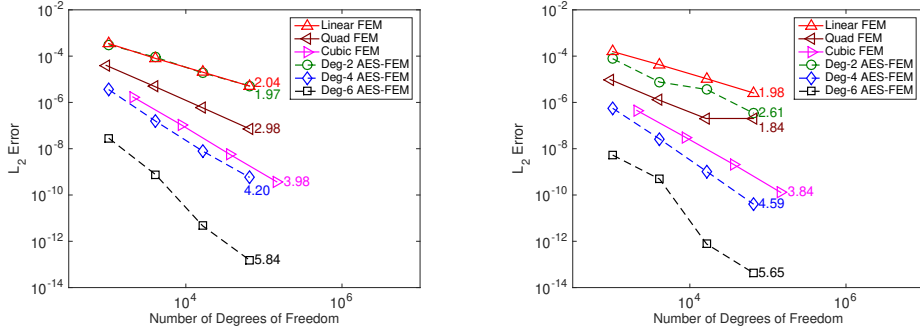


Figure 8: The  $L_2$  norm errors for 2D convection-diffusion equation on the unit square for  $U_2$  (left) and  $U_3$  (right).

We take  $\mathbf{c} = [1, 1]^T$  for all of our tests, and we consider the same analytic solutions over the unit square and on the unit circle as for the Poisson equation.

Figure 7 shows the  $L_\infty$  and  $L_2$  norm errors for  $U_1$  on the unit square. The  $L_2$  norm errors for  $U_2$  and  $U_3$  on the unit square and for  $U_3$  and  $U_4$  on the unit circle are shown in Figures 8 and 9, respectively. Similar to the Poisson equation, quadratic AES-FEM has similar convergence rate as linear FEM, but slightly lower errors. Quartic AES-FEM is more accurate than cubic FEM in all cases, and sextic AES-FEM again delivers superior accuracy, achieving about sixth-order convergence.

### 5.1.3 Assessment of Element-Quality Dependence

To assess the dependence of AES-FEM and FEM on mesh quality, we use a series of meshes for the unit square with progressively worse element quality, which we obtain by distorting a good-quality mesh. For AES-FEM and linear

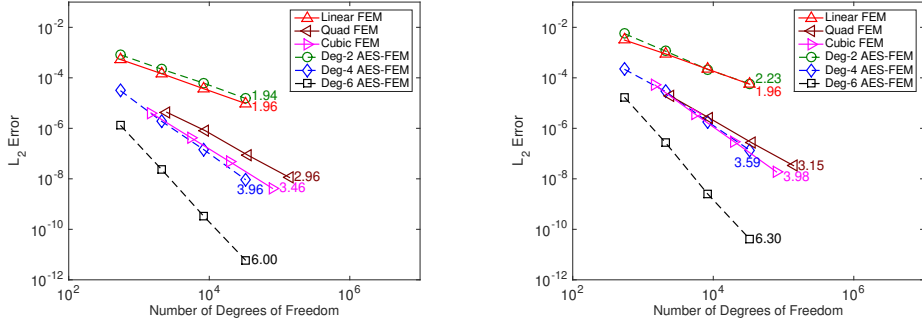


Figure 9: The  $L_2$  norm errors for 2D convection-diffusion equation on the unit circle for  $U_3$  (left) and  $U_4$  (right).

FEM, we use a mesh with 130,288 elements and 65,655 nodes and distort four elements by moving one vertex of each of these elements incrementally towards its opposite edge. For quadratic FEM, we use a mesh with 32,292 elements and 261,597 nodes and distort four elements by moving the vertices of each of these elements and their adjacent mid-edge nodes incrementally towards its opposite edge. For cubic FEM, we use a mesh with 32,292 elements and 146,077 nodes, and distort a single element by moving one vertex, its adjacent mid-edge nodes. On each distorted mesh, we solve the Poisson equation with the exact solution  $U_2$ .

Figure 10 shows the condition numbers of the stiffness matrices of FEM and AES-FEM and the numbers of iterations required to solve the linear systems. It can be seen that the condition numbers of FEM increase inversely proportional to the minimum angle, while the condition numbers of AES-FEM remain constant. In terms of the linear solver, the numbers of iteration increase significantly for linear FEM as the mesh is distorted, and preconditioned CG fails for poorly-shaped quadratic and cubic meshes due to nonpositive pivot during incomplete Cholesky or due to stagnation of CG. In contrast, the number of iterations remains constant for AES-FEM, independently of the element quality.

#### 5.1.4 Efficiency

To compare the efficiency of AES-FEM and FEM, Figures 11 and 12 show the errors versus runtimes for the 2D Poisson equation and convection-diffusion equation, respectively. It is evident that for the convection-diffusion equation, both quartic and sextic AES-FEM outperform cubic FEM over relatively fine meshes. For the Poisson equation, sextic AES-FEM outperforms cubic FEM over finer meshes. We expect AES-FEM will perform even better with further optimization of its implementation.

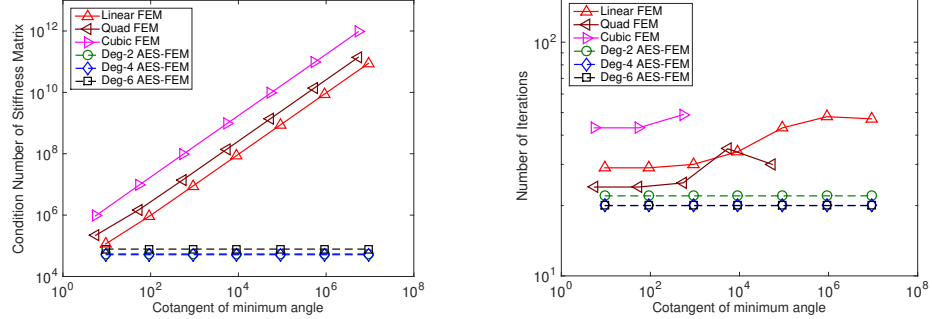


Figure 10: Left: the lower bound of the condition numbers of the stiffness matrices of FEM and AES-FEM method on a series of progressive worse meshes in 2D. Right: the number of iterations required for the iterative solver to converge when solving the corresponding systems.

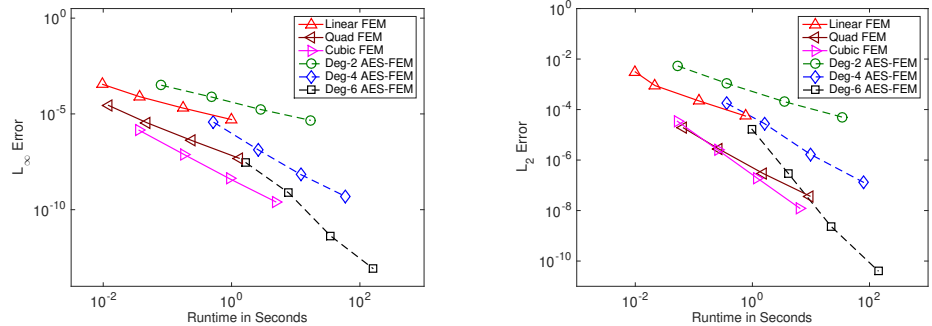


Figure 11: The errors verses runtime for 2D Poisson equation on the unit square for exact solution  $U_2$  (left) and on the unit circle for exact solution  $U_4$  (right).

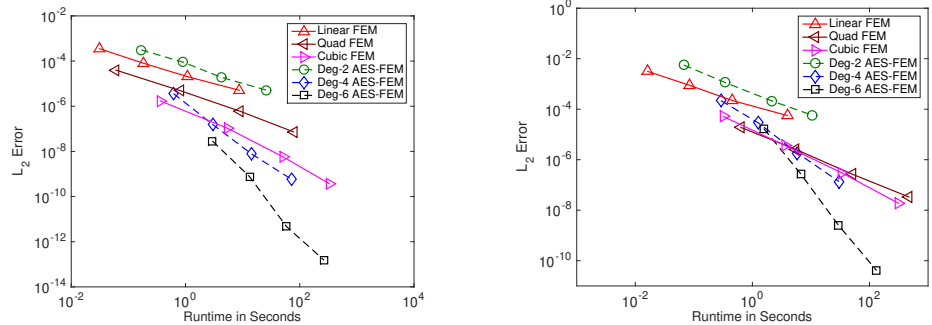


Figure 12: The errors verses runtime for 2D convection-diffusion equation on the unit square for exact solution  $U_2$  (left) and on the unit circle for exact solution  $U_4$  (right).

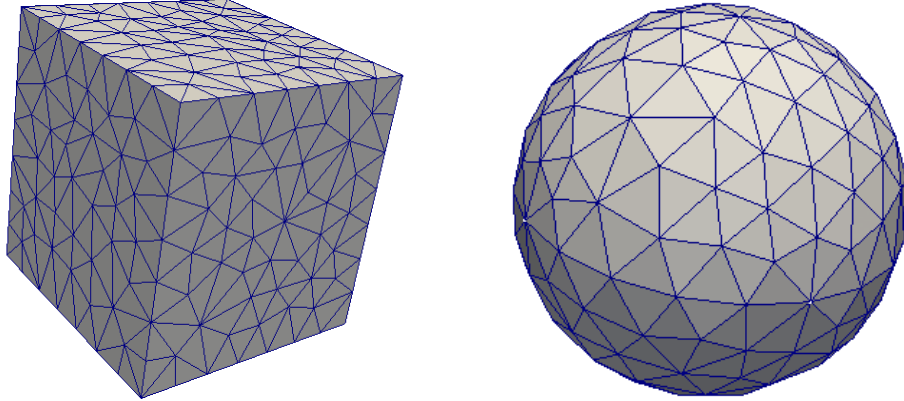


Figure 13: Example 3D meshes with linear elements.

## 5.2 3D Results

We now assess AES-FEM in 3D over the unit cube and the unit sphere, which are representative for geometries with flat and curved boundaries, respectively. We mesh the domains using TenGen [30] for the linear meshes and using Gmsh for the quadratic and cubic meshes. See Figure 13 for some example meshes with linear elements, which are representative in terms of mesh quality but are coarser than those used in actual computations. The numbers of nodes for the unit cube range from 509 to 7,272,811, and those for the unit sphere range from 1,011 to 2,834,229. As in 2D, since isoparametric FEM requires good mesh quality, we ensured that these meshes all have reasonable element shapes: For linear meshes, the minimum dihedral angle is 6.09 degrees and the maximum angle is 166.05 degrees; for high-order meshes, all elements have positive Jacobians everywhere.

We consider the Poisson equation and the convection-diffusion equation. For both cases, we use GMRES with the Gauss-Seidel preconditioner to solve the linear systems arising from AES-FEM. For FEM, we use CG with incomplete Cholesky as the preconditioner for the Poisson equation, and use GMRES with Gauss-Seidel for the convection-diffusion equation. We set the tolerance of the iterative solvers to  $10^{-12}$ . The drop tolerance for incomplete Cholesky is  $10^{-3}$  on the cube and  $10^{-6}$  on the sphere.

### 5.2.1 Poisson Equation

We first present results for the Poisson equation with Dirichlet boundary conditions on the unit cube and on the unit sphere. That is,

$$-\nabla^2 U = \rho \quad \text{in } \Omega, \quad (34)$$

$$U = g \quad \text{on } \partial\Omega. \quad (35)$$

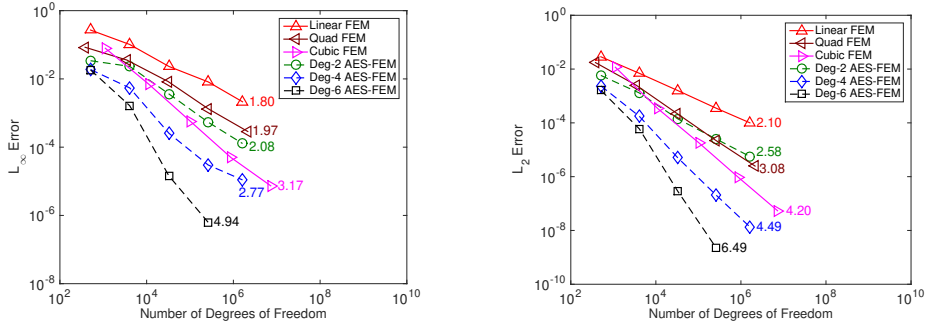


Figure 14: The errors for 3D Poisson equation on the unit cube for  $U_1$  in the infinity norm (left) and  $L_2$  norm (right).

For the unit cube, where  $\Omega = [0, 1]^3$ , we consider the following three analytic solutions:

$$U_1 = 64x^3(1 - x^3)y^3(1 - y^3)z^3(1 - z^3), \quad (36)$$

$$U_2 = \cos(\pi x)\cos(\pi y)\cos(\pi z), \quad (37)$$

$$U_3 = \frac{\sinh(\pi x)\cosh(\pi y)\cosh(\pi z)}{\sinh \pi \cosh^2 \pi}. \quad (38)$$

For the unit sphere  $\Omega = \{(x, y, z) | x^2 + y^2 + z^2 \leq 1\}$ , we consider the analytic solution  $U_4$  and also

$$U_4 = \cos\left(\frac{\pi}{2}(x^2 + y^2 + z^2)\right).$$

For each problem, the right-hand side  $\rho$  and the Dirichlet boundary conditions  $g$  are obtained from the given analytic solutions.

Figure 14 shows the  $L_\infty$  and  $L_2$  norm errors for  $U_1$  on the unit cube. The  $L_2$  norm errors for  $U_2$  and  $U_3$  on the unit cube and for  $U_3$  and  $U_4$  on the unit sphere are in Figures 15 and 16, respectively. In all cases, quadratic AES-FEM converges at similar or better rates than linear FEM and has lower errors, and quartic AES-FEM has similar or lower errors than cubic FEM. As in 2D, both of the aforementioned pairs have similar sparsity patterns and similar numbers of nonzeros in the coefficient matrices. Furthermore, sextic AES-FEM is far more accurate than all the other meshes, achieving sixth-order accuracy despite the use of linear elements. This further confirms our accuracy analysis in Section 4 for 3D problems.

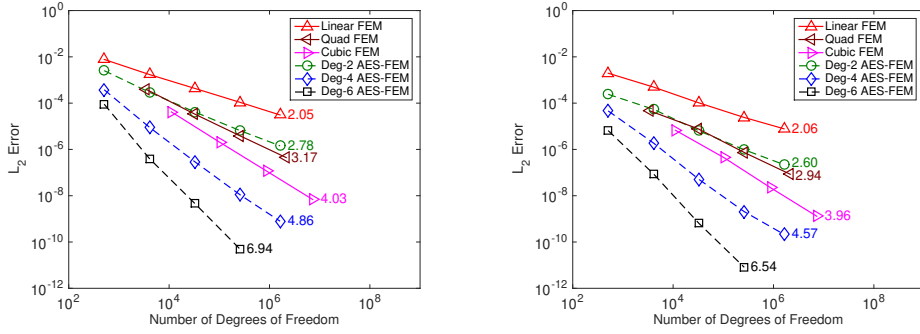


Figure 15: The  $L_2$  norm errors for 3D Poisson equation on the unit cube for  $U_2$  (left) and  $U_3$  (right).

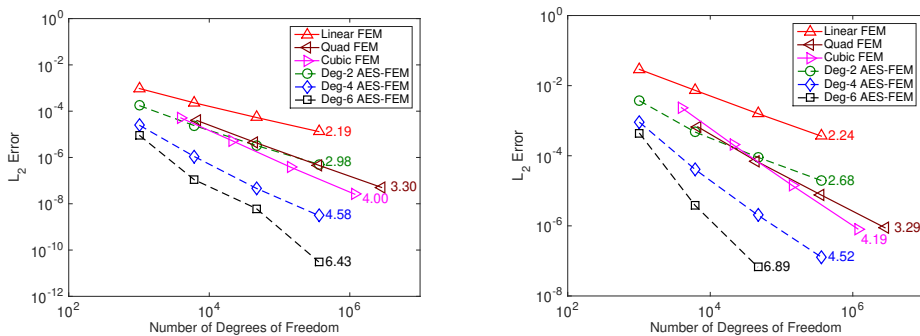


Figure 16: The  $L_2$  norm errors for 3D Poisson equation on the unit sphere for  $U_3$  (left) and  $U_4$  (right).

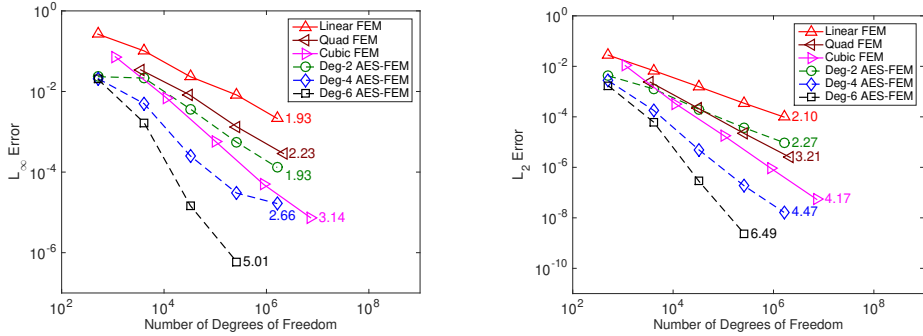


Figure 17: The errors for 3D convection-diffusion equation on the unit cube for  $U_1$  in the infinity norm (left) and  $L_2$  norm (right).

### 5.2.2 Convection-Diffusion Equation

We consider the time-independent convection-diffusion equation with Dirichlet boundary conditions on the unit cube and the unit sphere, that is,

$$-\nabla^2 U + \mathbf{c} \cdot \nabla U = \rho \quad \text{in } \Omega, \quad (39)$$

$$U = g \quad \text{on } \partial\Omega. \quad (40)$$

We take  $\mathbf{c} = [1, 1, 1]^T$  and we consider the same analytic solutions over the unit cube and unit sphere as for the Poisson equation.

Figure 17 shows the  $L_\infty$  and  $L_2$  norm errors for  $U_1$  on the unit cube. The  $L_2$  norm errors for  $U_2$  and  $U_3$  on the unit cube and for  $U_3$  and  $U_4$  on the unit sphere are in Figures 18 and 19, respectively. Similar to the Poisson equation, quadratic AES-FEM and linear FEM converge at similar rates with quadratic AES-FEM having slightly lower errors. Quartic AES-FEM is more accurate than the cubic FEM in all cases, and sextic AES-FEM is again the most accurate, with about sixth-order convergence. For FEM, the linear solver stagnated for the same problems on the finest mesh, but the resulting errors were small enough not to affect the comparison qualitatively.

### 5.2.3 Assessment of Element-Quality Dependence

To assess the dependence of AES-FEM and FEM on mesh quality in 3D, we use a series of meshes on the unit cube with progressively worse element quality, which we obtain by distorting a good-quality mesh. For AES-FEM and linear FEM, we use a mesh with 1,604,418 elements and 190,978 nodes and distort 74 elements by moving one vertex of each of these elements incrementally towards its opposite face. For quadratic FEM, we use a mesh with 178,746 elements and 250,047 nodes and distort nine elements by moving one vertex of each of

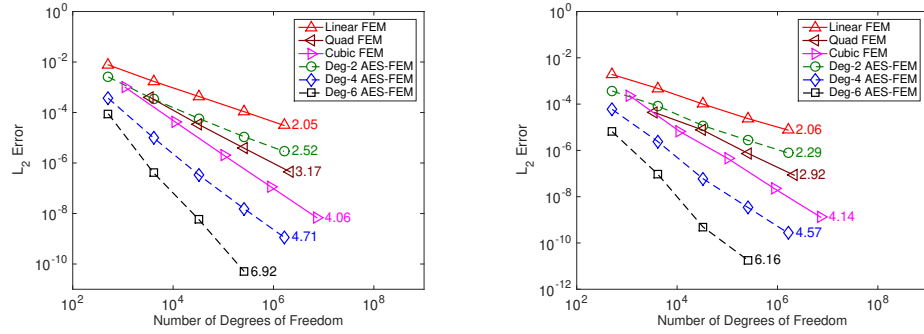


Figure 18: The  $L_2$  norm errors for 3D convection-diffusion equation on the unit cube for  $U_2$  (left) and  $U_3$  (right).

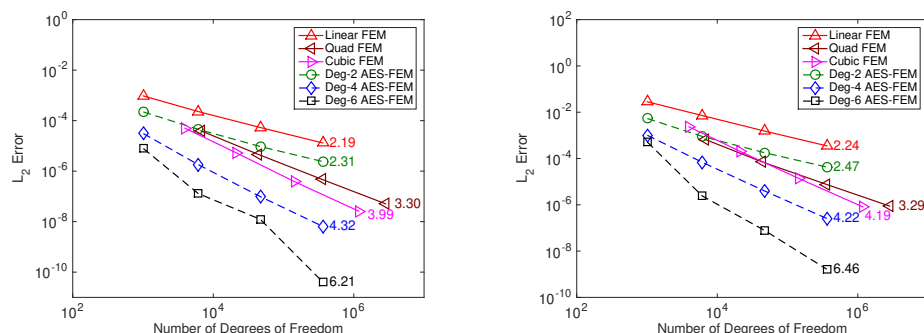


Figure 19: The  $L_2$  norm errors for 3D convection-diffusion equation on the unit sphere for  $U_3$  (left) and  $U_4$  (right).

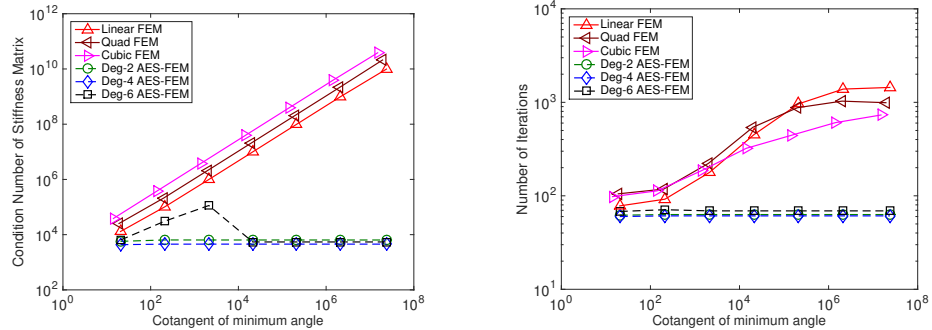


Figure 20: Left: the estimated condition numbers of the stiffness matrices of FEM and AES-FEM method on a series of progressive worse meshes in 3D. Right: the number of iterations required for the iterative solver to converge when solving the corresponding systems.

these elements and their adjacent mid-edge and mid-face nodes incrementally towards its opposite face. For cubic FEM, a mesh with 20,250 elements and 97,336 nodes is used and distort a single element by moving one vertex and its adjacent mid-edge, mid-face, and mid-cell nodes incrementally towards its opposite face.

On each distorted mesh, we solve the Poisson equation with the exact solution  $U_2$ . The iterative solvers used are GMRES for AES-FEM and CG for FEM. The tolerance for both solvers is  $10^{-8}$ . The preconditioner used for both methods is Gauss-Seidel.

Figure 20 shows the condition numbers of the stiffness matrices of FEM and AES-FEM and the numbers of iterations required to solve the linear systems. It can be seen that the condition numbers of FEM increase inversely proportional to the minimum angle, while the condition numbers of quadratic and quartic AES-FEM remain constant. The condition numbers of sextic AES-FEM increase slightly for the second and third meshes, but then dropped back to the original number. In terms of the linear solver, the number of iterations increases significantly for FEM while remaining constant for AES-FEM, independent of element quality.

#### 5.2.4 Efficiency

To compare the efficiency of AES-FEM and FEM in 3D, Figures 21 and 22 show the errors versus runtimes for the 3D Poisson equation and convection-diffusion equation, respectively. It is evident that on relatively finer meshes, sextic AES-FEM outperforms cubic FEM, and for the Poisson equation on the unit sphere, quartic AES-FEM does as well. We expect AES-FEM will perform even better with further code optimizations.

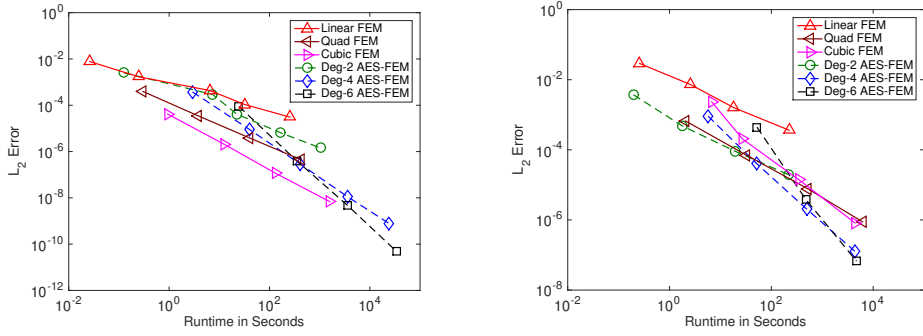


Figure 21: The errors verses runtime for 3D Poisson equation on the unit cube for exact solution  $U_2$  (left) and on the unit sphere for exact solution  $U_4$  (right).

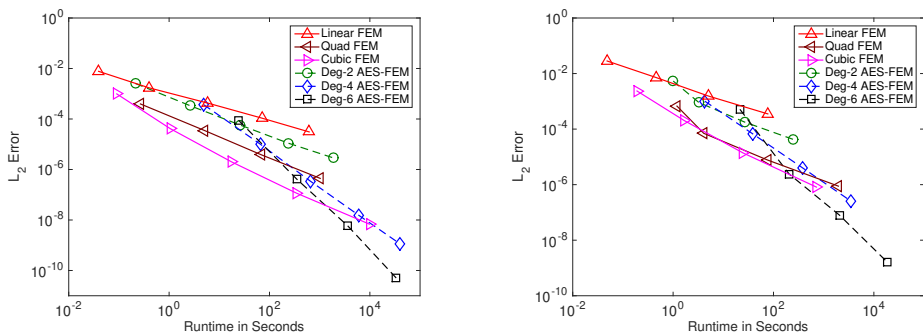


Figure 22: The errors verses runtime for 3D convection-diffusion equation on the unit cube for exact solution  $U_2$  (left) and on the unit sphere for exact solution  $U_4$  (right).

## 6 Conclusions and Future Work

In this paper, we presented a high-order extension of the adaptive extended stencil finite element method (AES-FEM). AES-FEM uses generalized Lagrange polynomial basis functions constructed from weighted least-squares approximations and utilizes meshes with linear elements. The method is independent of element quality and preserves the theoretical framework of the classical FEM. Additionally, essential boundary conditions and integrating the stiffness matrix can be performed in the same fashion as FEM. We compared the accuracy of quadratic, quartic and sextic AES-FEM against linear, quadratic and cubic FEM for the Poisson equation and the time-independent convection-diffusion equation in 2D and 3D, including on domains with curved boundaries. We showed improved accuracy and stability of high-order AES-FEM over high-order FEM. We demonstrated up to sixth order convergence rates of AES-FEM, despite the use of linear elements. In addition, the condition number of the stiffness matrix resulting from AES-FEM, and hence the number of iterations required to solve the system, is independent of the element quality. Additionally, we demonstrated that AES-FEM is more efficient on finer meshes than FEM in terms of error versus runtime.

While AES-FEM is efficient in terms of error versus runtime, it is slower than the classical FEM on a given mesh due to the more expensive computation of the basis functions and the non-symmetry of the stiffness matrix. The efficiency can be improved substantially by exploring  $p$ -adaptivity, leveraging the parallelism and the efficient multigrid solvers, which we will report in the future. Our present implementation of AES-FEM uses the standard hat functions as the weight functions, which may lead to large errors when applied to tangled meshes with inverted elements. We will report the resolution of tangled meshes in a future publication. This work has focused on elliptic or diffusion-dominant PDEs with solutions with smooth solutions. Another future research direction is the resolution of discontinuities from hyperbolic problems.

## Acknowledgements

Results were obtained using the high-performance LIred computing system at the Institute for Advanced Computational Science at Stony Brook University, which was obtained through the Empire State Development grant NYS #28451.

## References

- [1] D. N. ARNOLD, F. BREZZI, B. COCKBURN, AND L. D. MARINI, *Unified analysis of discontinuous Galerkin methods for elliptic problems*, SIAM J. Numer. Anal., 39 (2002), pp. 1749–1779.
- [2] I. BABUSKA, B. A. SZABO, AND I. N. KATZ, *The  $p$ -version of the finite element method*, SIAM J. Numer. Anal., 18 (1981), pp. 515–545.

- [3] F. BASSI AND S. REBAY, *A high-order accurate discontinuous finite element method for the numerical solution of the compressible Navier–Stokes equations*, J. Comput. Phys., 131 (1997), pp. 267–279.
- [4] F. BASSI AND S. REBAY, *High-order accurate discontinuous finite element solution of the 2D Euler equations*, J. Comput. Phys., 138 (1997), pp. 251–285.
- [5] T. BELYTSCHKO, Y. KRONGAUZ, D. ORGAN, M. FLEMING, AND P. KRYSL, *Meshless methods: An overview and recent developments*, Comput. Methods Appl. Mech. Engrg., 139 (1996), pp. 3–47.
- [6] C. CANUTO, M. Y. HUSSAINI, A. M. QUARTERONI, A. THOMAS JR, ET AL., *Spectral methods in fluid dynamics*, Springer Science & Business Media, Berlin Heidelberg, 2012.
- [7] B. COCKBURN, J. GOPALAKRISHNAN, AND R. LAZAROV, *Unified hybridization of discontinuous Galerkin, mixed, and continuous Galerkin methods for second order elliptic problems*, SIAM J. Numer. Anal., 47 (2009), pp. 1319–1365.
- [8] B. COCKBURN, G. E. KARNIADAKIS, AND C.-W. SHU, *The Development of Discontinuous Galerkin Methods*, Springer, 2000.
- [9] R. CONLEY, T. J. DELANEY, AND X. JIAO, *Overcoming element quality dependence of finite elements with adaptive extended stencil FEM (AES-FEM)*, Int. J. Numer. Meth. Engng., (2016). doi:10.1002/nme.5246.
- [10] L. DEMKOWICZ, W. RACHOWICZ, AND P. DEVLOO, *A fully automatic hp-adaptivity*, SIAM J. Sci. Comput., 17 (2002), pp. 117–142.
- [11] V. DYEDOV, N. RAY, D. EINSTEIN, X. JIAO, AND T. J. TAUTGES, *AHF: Array-based half-facet data structure for mixed-dimensional and non-manifold meshes*, in Proceedings of the 22nd International Meshing Roundtable, Springer, Orlando, Florida, 2014, pp. 445–464.
- [12] I. ERGATOUDIS, B. IRONS, AND O. ZIENKIEWICZ, *Curved, isoparametric, “quadrilateral” elements for finite element analysis*, Int. J. Solids Struct., 4 (1968), pp. 31–42.
- [13] B. A. FINLAYSON, *The Method of Weighted Residuals and Variational Principles*, Academic Press, New York, 1973.
- [14] A. GARGALLO-PEIRÓ, X. ROCA, J. PERAIRE, AND J. SARRATE, *Defining quality measures for validation and generation of high-order tetrahedral meshes*, in Proceedings of the 22nd International Meshing Roundtable, Springer, 2014, pp. 109–126.
- [15] C. GEUZAINÉ AND J.-F. REMACLE, *Gmsh: A 3-d finite element mesh generator with built-in pre-and post-processing facilities*, Int. J. Numer. Meth. Engrg., 79 (2009), pp. 1309–1331.

- [16] G. H. GOLUB AND C. F. VAN LOAN, *Matrix Computations*, Johns Hopkins, Baltimore, 4th ed., 2013.
- [17] T. J. HUGHES, J. A. COTTRELL, AND Y. BAZILEVS, *Isogeometric analysis: CAD, finite elements, NURBS, exact geometry and mesh refinement*, Comput. Meth. Appl. Mech. Engrg., 194 (2005), pp. 4135–4195.
- [18] X. JIAO AND H. ZHA, *Consistent computation of first-and second-order differential quantities for surface meshes*, in ACM Symposium on Solid and Physical Modeling, ACM, 2008, pp. 159–170.
- [19] A. JOHNEN, J.-F. REMACLE, AND C. GEUZAIN, *Geometrical validity of curvilinear finite elements*, J. Comput. Phys., 233 (2013), pp. 359–372.
- [20] M. LENOIR, *Optimal isoparametric finite elements and error estimates for domains involving curved boundaries*, SIAM J. Numer. Anal., 23 (1986), pp. 562–580.
- [21] J. T. ODEN, C. A. M. DUARTE, AND O. C. ZIENKIEWICZ, *A new cloud-based hp finite element method*, Comput. Methods Appl. Mech. Engrg., 153 (1998), pp. 117–126.
- [22] R. PASQUETTI AND F. RAPETTI, *Spectral element methods on triangles and quadrilaterals: comparisons and applications*, J. Comput. Phys., 198 (2004), pp. 349–362.
- [23] ———, *Spectral element methods on unstructured meshes: which interpolation points?*, Numer. Algorithms, 55 (2010), pp. 349–366.
- [24] A. T. PATERA, *A spectral element method for fluid dynamics: Laminar flow in a channel expansion*, J. Comput. Phys., 54 (1984), pp. 468–488.
- [25] J. PERAIRE AND P.-O. PERSSON, *The compact discontinuous Galerkin (CDG) method for elliptic problems*, SIAM J. Sci. Comput., 30 (2008), pp. 1806–1824.
- [26] P.-O. PERSSON AND J. PERAIRE, *Curved mesh generation and mesh refinement using Lagrangian solid mechanics*, in Proceedings of the 47th AIAA Aerospace Sciences Meeting and Exhibit, vol. 204, 2009.
- [27] N. RAY, D. WANG, X. JIAO, AND J. GLIMM, *High-order numerical integration over discrete surfaces*, SIAM J. Numer. Anal., 50 (2012), pp. 3061–3083.
- [28] R. SEVILLA, S. FERNÁNDEZ-MÉNDEZ, AND A. HUERTA, *NURBS-enhanced finite element method (NEFEM)*, Int. J. Numer. Meth. Engrg., 76 (2008), pp. 56–83.
- [29] J. R. SHEWCHUK, *Triangle: Engineering a 2D quality mesh generator and Delaunay triangulator*, in Applied Computational Geometry Towards Geometric Engineering, Springer, 1996, pp. 203–222.

- [30] H. ŠÍ, *TetGen, a Delaunay-based quality tetrahedral mesh generator*, ACM Trans. Math. Software, 41 (2015), pp. 11:1 – 11:36.
- [31] P. ŠOLÍN, J. ČERVENÝ, AND I. DOLEŽEL, *Arbitrary-level hanging nodes and automatic adaptivity in the hp-FEM*, Math. Comput. Simulat., 77 (2008), pp. 117–132.
- [32] P. ŠOLÍN, K. SEGETH, AND I. DOLEŽEL, *Higher-order finite element methods*, CRC Press, 2003.
- [33] B. SZABO AND A. MEHTA, *p-convergent finite element approximations in fracture mechanics*, Int. J. Numer. Meth. Engng., 12 (1978), pp. 551–560.
- [34] M. A. TAYLOR AND B. WINGATE, *A generalized diagonal mass matrix spectral element method for non-quadrilateral elements*, Appl. Numer. Math., 33 (2000), pp. 259–265.
- [35] T. TOULORGE, C. GEUZAIN, J.-F. REMACLE, AND J. LAMBRECHTS, *Robust untangling of curvilinear meshes*, J. Comput. Phys., 254 (2013), pp. 8–26.
- [36] P. VINCENT AND A. JAMESON, *Facilitating the adoption of unstructured high-order methods amongst a wider community of fluid dynamicists*, Math. Model. Nat. Phenom., 6 (2011), pp. 97–140.
- [37] D. WANG, B. CLARK, AND X. JIAO, *An analysis and comparison of parameterization-based computation of differential quantities for discrete surfaces*, Comput. Aid. Geom. Des., 26 (2009), pp. 510–527.
- [38] Z. WANG, *High-order methods for the Euler and Navier–Stokes equations on unstructured grids*, Prog. Aerosp. Sc., 43 (2007), pp. 1–41.
- [39] N. ZANDER, T. BOG, S. KOLLMANNSSBERGER, D. SCHILLINGER, AND E. RANK, *Multi-level hp-adaptivity: high-order mesh adaptivity without the difficulties of constraining hanging nodes*, Comput. Mech., 55 (2015), pp. 499–517.
- [40] O. ZIENKIEWICZ, R. TAYLOR, AND J. ZHU, *The Finite Element Method: Its Basis and Fundamentals*, Butterworth-Heinemann, Oxford, 7th ed., 2013.